Probing Rotated Weyl Physics on Nonlinear Lithium Niobate-on-Insulator Chips

Zhi-Wei Yan,[1,*] Qiang Wang,[2,*] Meng Xiao,[3,†] Yu-Le Zhao,[1] Shi-Ning Zhu,[1] and Hui Liu[1,‡]

[1]*National Laboratory of Solid State Microstructures, School of Physics, Collaborative Innovation Center of Advanced Microstructures, Nanjing University, Nanjing 210093, China*

[2]*Division of Physics and Applied Physics, School of Physical and Mathematical Sciences, Nanyang Technological University, Singapore 637371, Singapore*

[3]*Key Laboratory of Artificial Micro- and Nano-Structures of Ministry of Education and School of Physics and Technology, Wuhan University, Wuhan 430072, China*

(Received 22 January 2021; accepted 27 May 2021; published 1 July 2021)

Topological photonics, featured by stable topological edge states resistant to perturbations, has been utilized to design robust integrated devices. Here, we present a study exploring the intriguing topological rotated Weyl physics in a 3D parameter space based on quaternary waveguide arrays on lithium niobate-on-insulator (LNOI) chips. Unlike previous works that focus on the Fermi arc surface states of a single Weyl structure, we can experimentally construct arbitrary interfaces between two Weyl structures whose orientations can be freely rotated in the synthetic parameter space. This intriguing system was difficult to realize in usual 3D Weyl semimetals due to lattice mismatch. We found whether the interface can host gapless topological interface states or not is determined by the relative rotational directions of the two Weyl structures. In the experiment, we have probed the local characteristics of the TISs through linear optical transmission and nonlinear second harmonic generation. Our study introduces a novel path to explore topological photonics on LNOI chips and various applications in integrated nonlinear and quantum optics.

DOI: 10.1103/PhysRevLett.127.013901

Introduction.—Since the discovery of the quantum Hall effect [1,2], topological materials have been discovered in various physical systems, such as topological insulators [3,4], topological semimetals [5], graphene [6], etc. The most interesting property of these topological materials is the existence of topologically protected edge states or surface states, for example, the Fermi arc surface states in Weyl semimetals. At present, the Weyl point (WP) has been observed in condensed matters [7,8], photonic crystals [9,10], waveguide arrays [11], and metamaterials [12–14]. In addition, with the help of synthetic dimension, people can also obtain 3D WPs with lower dimensional structures [15,16]. Although Weyl semimetals have been widely studied, most of the researches have focused on the single Weyl crystal [7–16]. Recently, rotating bilayer graphene has become a hot topic [17]. However, the topological physics of two rotating Weyl structures has never been studied. According to our knowledge, topological interface states (TISs) between two independent Weyl structures have not been realized yet. It is because the construction of interface in condensed matters, photonic crystals, optical lattices, and metamaterials is quite challenging, which requires lattice matching and specific crystal orientation.

Branching from topological insulators, topological photonics [18–20], which hosts topological edge states [21–27], has been utilized to design robust integrated optical devices. One of the ideal platforms is the silicon-on-insulator (SOI), where various integrated topological devices have been experimentally realized [28–32], including waveguide lattices, ring resonator arrays, and photonic crystals. Besides SOI, lithium niobate-on-insulator (LNOI), as a new promising integrated-photonics platform, has attracted increasing attention due to its remarkable characteristics [33–37]. Compared with SOI, LNOI has several advantages, for instance, high second-order nonlinearity, strong electro-optic effect, and transparency in the visible region. Although some microstructures in LNOI have been reported to obtain various integrated photonic devices, including waveguides, resonant cavities, and periodically poled lithium niobate (LN) structures [33–37], the territory of topological photonics on LNOI chips remains largely unexplored.

In this work, we propose an experimental study exploring synthetic rotated Weyl physics based on quaternary waveguide arrays (QWAs) on a LNOI chip. A feasible strategy is used to construct arbitrary interface between two independent Weyl structures. The interface can either host gapless TISs or not, depending on the relative rotational directions of the two Weyl structures. If they rotate in opposite directions, two types of gapless TISs arise. Otherwise, if they rotate in the same direction, only a trivial interface state can exist. In experiments, we designed and fabricated spliced LNOI QWAs, and observed the TISs through linear and nonlinear optical measurements.

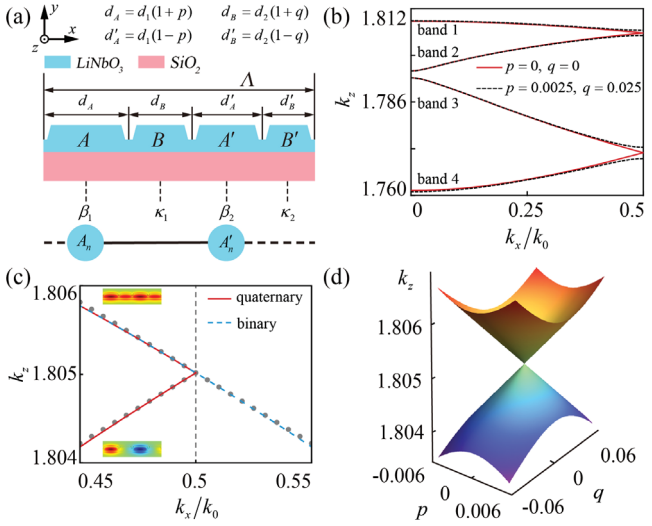

FIG. 1. Realization of a WP by the 1D QWA. (a) Schematic of a 1D QWA in a unit cell that consists of four waveguides, with 370 nm in height and a 65° sidewall angle. p and q are two independent numbers forming a parameter space. (b) Band dispersions at a fixed wavelength ($\lambda = 1040$ nm). Here, $k_0 = \pi/(d_1 + d_2)$ and k_z is normalized by $2\pi/\lambda$. (c) The band dispersions of the QWA ($p = q = 0$) around the crossing formed by bands 1 and 2 in (b), where the solid red lines are calculated in the frame of a QWA, while the dashed blue line is from a binary waveguide array. The solid gray dots are numerical results obtained by the tight-binding approximation. (d) The band structure in the (p, q) space with $k_x = 0.5k_0$ forms a conical intersection.

Lithium niobate-on-insulator quaternary waveguide arrays.—Figure 1(a) shows the cross section of a LNOI QWA in a unit cell, which consists of four waveguides with the widths defined as $d_A = d_1(1 + p)$, $d'_A = d_1(1 - p)$, $d_B = d_2(1 + q)$, and $d'_B = d_2(1 - q)$, where $d_1 = 1$ μm, $d_2 = 0.8$ μm, and the lattice constant is $\Lambda = 2d_1 + 2d_2$. p and q are two independent numbers within $(-1, 1)$, which construct a 3D synthetic parameter space [38] when incorporating the 1D Bloch wave vector k_x.

The first four band dispersions of the fundamental transverse magnetic modes at a fixed wavelength (1040 nm) calculated by COMSOL Multiphysics (COMSOL Inc.) are plotted in Fig. 1(b), where the longitudinal wave vector k_z acts as the effective "energy" and k_x is the 1D Bloch wave vector in unit of $k_0 = \pi/(d_1 + d_2)$. Considering the special case $p = q = 0$ as plotted with red lines, the QWA is equivalent to a binary waveguide array; thus, the two bands form a linear crossing at $k_x = 0.5k_0$ due to the band folding. The band dispersions near the crossing formed by bands 1 and 2 are enlarged in Fig. 1(c). Once deviating from $(p, q) = (0, 0)$, the degeneracy is lifted, and a band gap emerges [see the dashed black lines in Fig. 1(b)].

Considering bands 1 and 2, as most of the field distribution is located at the A and A' positions [see the inset of Fig. 1(c)], the $B(B')$ waveguides can be regarded as auxiliary waveguides to control the coupling strength between adjacent A and A' waveguides [39]. Then the QWA reduces to an effective binary optical lattice, as illustrated in the bottom of Fig. 1(a). By employing the tight-binding approximation, the Hamiltonian is

$$\begin{aligned} H = {} & \kappa_1(q)\sum_n (A_n^\dagger A'_n + A'^\dagger_n A_n) \\ & + \kappa_2(q)\sum_n (A_{n+1}^\dagger A'_n + A'^\dagger_n A_{n+1}) \\ & + \beta_1(p)\sum_n A_n^\dagger A_n + \beta_2(p)\sum_n A'^\dagger_n A'_n, \end{aligned} \tag{1}$$

where $\kappa_{1(2)}(q)$ represent two effective coupling coefficients that are functions of q, and $\beta_{1(2)}(p)$ are the on-site propagation constants of the $A(A')$ waveguides that are functions of p. For $(p, q) = (0, 0)$, the dispersions are plotted with gray dots in Fig. 1(c), which matches well with the simulation data. By expanding near the degenerate point $(p_w, q_w, k_w) = (0, 0, 0.5k_0)$, we can get the effective Hamiltonian (Supplemental Material, Sec. I [40]): $H = b\xi_p\sigma_z + 2m\xi_q v_{qx}\sigma_x - \kappa_0\xi_k\sigma_y + \beta_0\sigma_0$, where $\xi_p = p - p_w$, $\xi_q = q - q_w$, $\xi_k = (k - k_w)/k_0$ are three dimensionless coefficients, $\sigma_i (i = x, y, z)$ is the Pauli matrix, σ_0 is a 2×2 identity matrix, $\beta_0 = 1.805$, $b = 0.09$, $m = 0.018$, and $\kappa_0 = 0.009$. This Hamiltonian takes a standard Weyl Hamiltonian form [43]. Figure 1(d) shows the projection of the bulk bands in the (p, q) space with $k_x = 0.5k_0$. According to the definition [43], the degenerate point is actually a WP. Its 'charge' can be determined as $c = \mathrm{sgn}(-bm\kappa_0) = -1$. In addition to this WP corresponding to $A(A')$ waveguides, we can also find another WP related to $B(B')$ waveguides if we regard $A(A')$ waveguides as auxiliary waveguides (Supplemental Material, Sec. II [40]). In the following content, we only focus on the former WP. Fermi arclike edge states related to a single WP are observed (Supplemental Material, Sec. III [40]). As the parameter space is not periodic, charge neutrality is not indispensable here [16,41]. Thus, unlike periodic systems [7–16], our system exhibits a single negative-charged WP (Supplemental Material, Sec. IV [40]). This is a unique feature of synthetic dimension, which leads to incomparable advantages in controlling the surface states.

Rotated Weyl physics.—Here we propose a highly adjustable topological interface formed between two Weyl structures by rotating them in opposite directions. To define the rotation of them in the k_z direction, we consider two rotational loops in the two parameter spaces, as illustrated in Fig. 2(a):

$$\begin{cases} \xi_{p1} = r_1 \cos\varphi_1, \\ \xi_{q1} = r_2 \sin\varphi_1, \end{cases} \quad \begin{cases} \xi_{p2} = r_1 \cos\varphi_2, \\ \xi_{q2} = r_2 \sin\varphi_2, \end{cases} \tag{2}$$

where $\varphi_1, \varphi_2 \in [-\pi, \pi)$ are the rotational angles around WP1 and WP2, respectively, and r_1, r_2 are the shared radii.

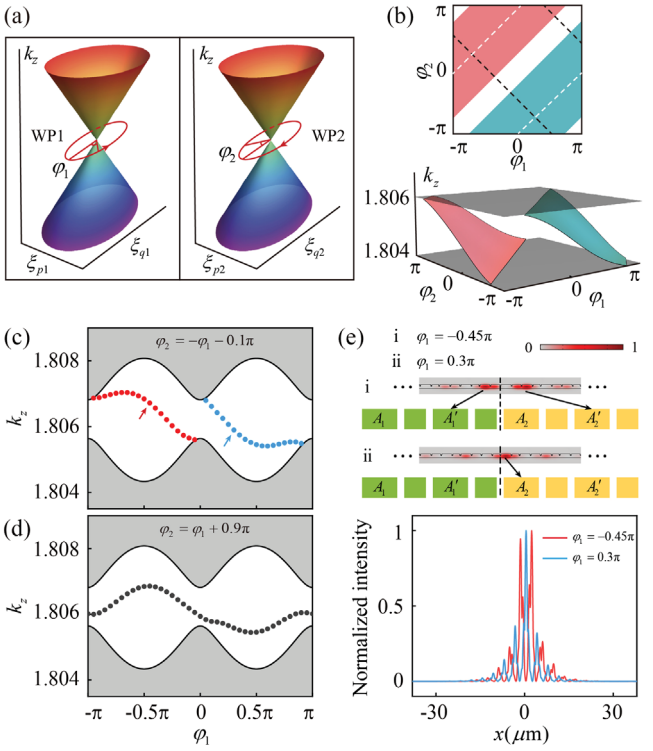

FIG. 2. TISs of the interfaced two WPs. (a) Interfacing two WPs. Two rotational loops of the same size encircling the WP are introduced in the parameter spaces. (b) Numerical results for small loops in (a), projected in the new (φ_1, φ_2) space (bottom). Top inset: the projection to the (φ_1, φ_2) plane, where the black dashed line leads to a nontrivial case while the white dashed line results in a trivial case. (c), (d) Eigenvalue spectra as a function of φ_1 by full-wave simulation for large loops in (a), which follow specific paths in (b): $\varphi_2 = -\varphi_1 - 0.1\pi$ [(c), rotating in the opposite directions, nontrivial], $\varphi_2 = \varphi_1 + 0.9\pi$ [(d), rotating in the same direction, trivial]. The gray regions represent bulk bands. (e) Top: field intensity distributions of the two types of TISs in (c) (indicated by the red and blue arrows). The eight central waveguides are enlarged. The black dashed line indicates the position of the interface. Bottom: the corresponding field intensity profiles.

In such a way, we can map the original two "independent" WPs to a new (φ_1, φ_2) parameter space. Numerical calculations based on the tight-binding model are carried out for the compound interfaced structure, in which $r_1 = 0.0045$, $r_2 = 0.045$, and the number of unit cells is set as 100 at each side. Figure 2(b) shows the eigenvalue spectrum in the (φ_1, φ_2) space. Two colored surfaces representing two types of interface states connect the upper and lower bulk bands. We project them to the (φ_1, φ_2) plane in the top inset. If the two Weyl structures rotate in opposite directions, we can define the relationship between the two angles as $\varphi_2 = -\varphi_1 + \theta$ (Supplemental Material, Sec. V [40]), where θ is a constant, as illustrated by the dashed black line under periodic conditions. In this situation the topological charges of the WPs are opposite (Supplemental Material, Sec. VI [40]). The loop around WP1 exhibits a counterclockwise rotation, while the loop encircling WP2 follows a clockwise rotation, as illustrated by the arrows in Fig. 2(a). According to the bulk-edge correspondence [20], there must exist two TISs on the interface.

For further verification, we perform full-wave simulations following the path $\varphi_2 = -\varphi_1 - 0.1\pi$ in the compound system, where $r_1 = 0.03$ and $r_2 = 0.125$, and the number of unit cells is set as 10 at each side. Figure 2(c) shows the eigenvalue spectrum as a function of φ_1, where the gray regions represent bulk bands. Two types of gapless TISs are plotted with solid red and blue dots. We choose two cases for illustration purposes [indicated by arrows in Fig. 2(c)] and plot the field intensity distributions and profiles in Fig. 2(e). For $\varphi_1 = -0.45\pi$, the interface mode has strong field confinement in the vicinity of the interface, with the majority of field intensities lying on the central A_1' and A_2' waveguides. For $\varphi_1 = 0.3\pi$, an exponentially localized intensity profile is revealed, with the maximum field intensity lying on the central A_2 waveguide. Note that we only choose $\theta = -0.1\pi$ for $\varphi_2 = -\varphi_1 + \theta$ above. Other values of θ are also analyzed in the Supplemental Material, Sec. VII [40], where the phenomenon of two gapless TISs is maintained. This indicates that the interface we constructed shows great flexibility, owing to that $\xi_{p1(2)}$ and $\xi_{q1(2)}$ are synthetic momentum vectors.

Note that we only go through the curve of a fixed same size encircling each WP in the $(\xi_{p1(2)}, \xi_{q1(2)})$ spaces. The new $(\varphi_1, \varphi_2, k_x)$ parameter space is a 3D space, where each 2D (φ_1, k_x) slice that does not contain any Weyl nodes can be considered as a Chern insulator. The Chern number changes by two following the $\varphi_2 = -\varphi_1 + \theta$ loop, leading to two gapless TISs. If we sweep the radii of the loops, fermi arclike interface states can be obtained. Here, the relative rotational directions determine the topological charges of Weyl nodes. On the contrary, if two Weyl nodes rotate in the same direction as $\varphi_2 = \varphi_1 + \theta'$ [see the dashed white line in Fig. 2(b)] (Supplemental Material, Sec. V [40]), the topological charges are the same (Supplemental Material, Sec. VIII [40]). Figure 2(d) shows an example of $\varphi_2 = \varphi_1 + 0.9\pi$. The Chern number does not change in this situation, leading to no gapless TISs, which is a trivial case. Similar phenomena take place for other values of θ'.

Experimental observation of topological interface states.—We propose the LNOI QWAs for exploring the TISs (Supplemental Material, Sec. IX [40]). Three compound QWAs were fabricated corresponding to $\varphi_1 = -0.45\pi, 0.3\pi, \pi$, where $\varphi_2 = -\varphi_1 - 0.1\pi$. The scanning electron microscopy images of one sample are presented in Figs. 3(a) and 3(b). In the experiments, we input the 1040-nm light into the QWAs and captured the output signals, which are displayed in Figs. 3(d), 3(f), and 3(h) (top panels). Their intensity profiles are displayed in bottom panels with solid black curves. For verification, numerical propagation simulations are performed in Figs. 3(c),3(e),

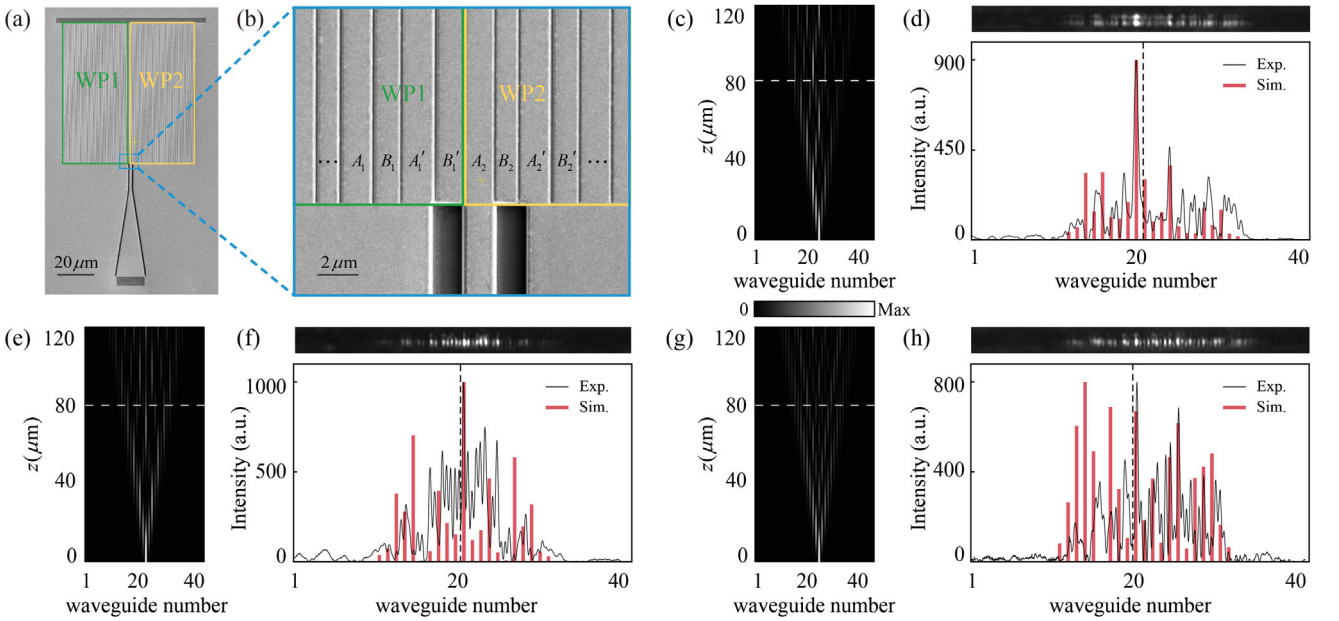

FIG. 3. Numerical and experimental results. (a) Scanning electron microscopy top view of a sample. (b) Enlarged regions in (a). (c), (e),(g) Propagation simulations. TISs cases: $\varphi_1 = -0.45\pi$ (c), $\varphi_1 = 0.3\pi$ (e); Case without TIS: $\varphi_1 = \pi$ (g), where $\varphi_2 = -\varphi_1 - 0.1\pi$. The gray color range is. [0,0.4]. (d),(f),(h) Experimentally detected output intensities (top) and intensity profiles (bottom) of simulation results (red bars) and experimental results (solid curves) for different cases: $\varphi_1 = -0.45\pi$ (d), $\varphi_1 = 0.3\pi$ (f), $\varphi_1 = \pi$ (h). The intensities are all normalized to the specific photoelectric conversion parameter of the sCMOS camera (Hamamatsu, ORCA-Flash 4.0, C11440-42U).

and 3(g). We extracted the intensity of simulations at the propagation length of experimental samples (indicated by the dashed white line) and displayed them in Figs. 3(d), 3(f), and 3(h) (bottom panels) with red bar diagrams.

For $\varphi_1 = -0.45\pi$, we take the central A_2' waveguide as the input, since the maximum field intensity of TIS lies on it [see Fig. 2(e)]. The simulation shows that most of the field intensity is located near the interface. Part of the field is spreading during the propagation, due to that the input mode is not a pure TIS, but a superposition of the TIS and other bulk modes. Figure 3(d) shows good agreement between experiment and simulation, with a power maximum near the interface (dashed black line) and an exponential decay on both sides. For $\varphi_1 = 0.3\pi$, we choose the central A_2 waveguide as the input. The propagation simulation in Fig. 3(e) shows a singular topological defect among spreading bulk modes. In Fig. 3(f), both the experiment and simulation exhibit a power maximum near the interface, with exponentially attenuated intensities away from it, which shows a reasonable match. For $\varphi_1 = \pi$, no TIS is supported. The simulation propagation behavior in Fig. 3(g) is manifested like the well-known phenomenon of discrete diffraction [42]. The light coupled into the central A_2' waveguide spreads as it propagates. The experimental measurement and the simulation follow the same diffused trends in Fig. 3(h).

The localization of light intensity near the interface indicates the existence of TISs, while the diffused light spread away from the interface shows the case without TIS (Supplemental Material, Sec. X [40]). We also perform numerical calculations with random disorders introduced to the three samples. The presence of two TISs accompanied by the absence of TIS during the sampling of adiabatic pumping process is consistent with the theoretical predication of two gapless TIS bands (Supplemental Material, Sec. XI [40]).

In addition to the experimental methods above, nonlinear optics can also provide a good method to probe TISs [32]. Here we use efficient second-harmonic generation (SHG) in LNOI to investigate TISs. With the same input positions as in the fundamental frequency (FF) light (1040 nm) cases, the captured SHG light (520 nm) at the output is shown in Fig. 4(a). We extracted the SHG intensity profiles and

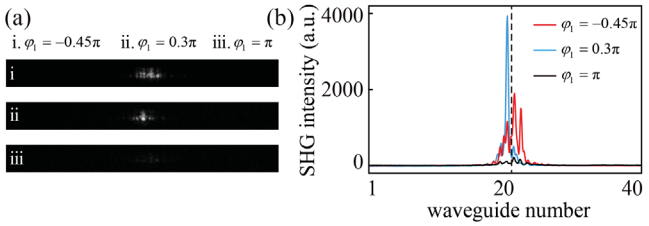

FIG. 4. Experimental second-harmonic generation (SHG) results. (a) Experimentally detected output SHG intensities for the three cases. (b) The corresponding SHG intensity profiles with colored solid curves. The intensities are all normalized to the specific photoelectric conversion parameter of the sCMOS camera (Hamamatsu, ORCA-Flash 4.0, C11440-42U).

plotted them with curves of different colors for the three cases in Fig. 4(b). The two TIS cases ($\varphi_1 = -0.45\pi, 0.3\pi$) exhibit a much stronger SHG signal than the case without TIS ($\varphi_1 = \pi$), indicating a nonlinear enhancement for TISs due to the strong field localization and the immunity to fabrication imperfections. Note that SHG light exhibits a more localized distribution than FF light, which is reasonable since the coupling strength of the SHG light is weaker than that of the FF light. The SHG signals provide another effective way to observe the field localization of TISs.

Conclusion and discussion.—In summary, we bridge topological photonics with the LNOI platform. We demonstrate rotated Weyl physics with QWAs on a LNOI chip. We successfully construct an interface between two rotated Weyl structures whose topological relations can be flexibly tuned. The interface between two Weyl structures with opposite rotational directions supports two gapless TISs, which were experimentally observed. The local characteristics of the TISs is also probed by nonlinear SHG. In this work, we only discuss the interface state between two rotating Weyl structures in the synthetic parameter space, and this result can possibly be extended to real 3D Weyl structures. However, we have to solve the problem of lattice matching when splicing two rotated 3D Weyl lattices. It can be anticipated that they can only match for some specific rotational angles, and the mismatch for an arbitrary rotational angle will inevitably introduce significant defects. Future research on this topic is worth exploring. Beyond this, it is possible to investigate the interface states between two non-Hermitian Weyl rings if gain and loss are considered [44]. Moreover, this work introduces a new way to study linear and nonlinear topological photonics on the LNOI platform and can lead to various applications in integrated nonlinear and quantum optics.

This work was financially supported by the National Key Research and Development Program of China (Grants No. 2017YFA0205700 and No. 2017YFA0303702), the National Natural Science Foundation of China (Grants No. 11690033 and No. 11904264) and the program B for Outstanding Ph.D. candidate of Nanjing University.

*Z.-W. Y. and Q. W. contributed equally to this work.
†Corresponding author.
phmxiao@whu.edu.cn
‡Corresponding author.
liuhui@nju.edu.cn

[1] K. V. Klitzing, G. Dorda, and M. Pepper, Phys. Rev. Lett. **45**, 494 (1980).
[2] K. von Klitzing, Rev. Mod. Phys. **58**, 519 (1986).
[3] M. Z. Hasan and C. L. Kane, Rev. Mod. Phys. **82**, 3045 (2010).
[4] X.-L. Qi and S.-C. Zhang, Rev. Mod. Phys. **83**, 1057 (2011).
[5] N. P. Armitage, E. J. Mele, and A. Vishwanath, Rev. Mod. Phys. **90**, 015001 (2018).
[6] A. H. Castro-Neto, F. Guinea, N. M. R. Peres, K. S. Novoselov, and A. K. Geim, Rev. Mod. Phys. **81**, 109 (2009).
[7] X. G. Wan, A. M. Turner, A. Vishwanath, and S. Y. Savrasov, Phys. Rev. B **83**, 205101 (2011).
[8] S. Y. Xu *et al.*, Science **349**, 613 (2015).
[9] L. Lu, Z. Wang, D. Ye, L. Ran, L. Fu, J. D. Joannopoulos, and M. Soljačić, Science **349**, 622 (2015).
[10] W. J. Chen, M. Xiao, and C. T. Chan, Nat. Commun. **7**, 13038 (2016).
[11] J. Noh, S. Huang, D. Leykam, Y. D. Chong, K. P. Chen, and M. C. Rechtsman, Nat. Phys. **13**, 611 (2017).
[12] M. Xiao, Q. Lin, and S. Fan, Phys. Rev. Lett. **117**, 057401 (2016).
[13] B. Yang *et al.*, Science **359**, 1013 (2018).
[14] R. Li, B. Lv, H. Tao, J. Shi, Y. Chong, B. Zhang, and H. Chen, Natl. Sci. Rev., nwaa192 (2020).
[15] Q. Lin, M. Xiao, L. Yuan, and S. Fan, Nat. Commun. **7**, 13731 (2016).
[16] Q. Wang, M. Xiao, H. Liu, S. Zhu, and C. T. Chan, Phys. Rev. X **7**, 031032 (2017).
[17] Y. Cao, V. Fatemi, S. Fang, K. Watanabe, T. Taniguchi, E. Kaxiras, and P. Jarillo-Herrero, Nature (London) **556**, 43 (2018).
[18] L. Lu, J. D. Joannopoulos, and M. Soljačić, Nat. Photonics **8**, 821 (2014).
[19] A. B. Khanikaev and G. Shvets, Nat. Photonics **11**, 763 (2017).
[20] T. Ozawa *et al.*, Rev. Mod. Phys. **91**, 015006 (2019).
[21] Z. Wang, Y. Chong, J. D. Joannopoulos, and M. Soljacic, Nature (London) **461**, 772 (2009).
[22] M. Hafezi, E. A. Demler, M. D. Lukin, and J. M. Taylor, Nat. Phys. **7**, 907 (2011).
[23] A. B. Khanikaev, S. H. Mousavi, W. K. Tse, M. Kargarian, A. H. MacDonald, and G. Shvets, Nat. Mater. **12**, 233 (2013).
[24] M. C. Rechtsman, J. M. Zeuner, Y. Plotnik, Y. Lumer, D. Podolsky, F. Dreisow, S. Nolte, M. Segev, and A. Szameit, Nature (London) **496**, 196 (2013).
[25] T. Ma and G. Shvets, New J. Phys. **18**, 025012 (2016).
[26] J. W. Dong, X. D. Chen, H. Zhu, Y. Wang, and X. Zhang, Nat. Mater. **16**, 298 (2017).
[27] S. Xia *et al.*, Phys. Rev. Lett. **121**, 263902 (2018).
[28] M. Hafezi, S. Mittal, J. Fan, A. Migdall, and J. M. Taylor, Nat. Photonics **7**, 1001 (2013).
[29] A. Blanco-Redondo, I. Andonegui, M. J. Collins, G. Harari, Y. Lumer, M. C. Rechtsman, B. J. Eggleton, and M. Segev, Phys. Rev. Lett. **116**, 163901 (2016).
[30] M. I. Shalaev, W. Walasik, A. Tsukernik, Y. Xu, and N. M. Litchinitser, Nat. Nanotechnol. **14**, 31 (2019).
[31] X. T. He, E. T. Liang, J. J. Yuan, H. Y. Qiu, X. D. Chen, F. L. Zhao, and J. W. Dong, Nat. Commun. **10**, 872 (2019).
[32] D. Smirnova, S. Kruk, D. Leykam, E. Melik-Gaykazyan, D. Y. Choi, and Y. Kivshar, Phys. Rev. Lett. **123**, 103901 (2019).
[33] G. Poberaj, H. Hu, W. Sohler, and P. Günter, Laser Photonics Rev. **6**, 488 (2012).

[34] A. Boes, B. Corcoran, L. Chang, J. Bowers, and A. Mitchell, Laser Photonics Rev. **12**, 1700256 (2018).
[35] C. Wang, M. Zhang, X. Chen, M. Bertrand, A. Shams-Ansari, S. Chandrasekhar, P. Winzer, and M. Loncar, Nature (London) **562**, 101 (2018).
[36] M. He *et al.*, Nat. Photonics **13**, 359 (2019).
[37] J. Lin *et al.*, Phys. Rev. Lett. **122**, 173903 (2019).
[38] L. Q. Yuan, Q. Lin, M. Xiao, and S. H. Fan, Optica **5**, 1396 (2018).
[39] M. Mrejen, H. Suchowski, T. Hatakeyama, C. Wu, L. Feng, K. O'Brien, Y. Wang, and X. Zhang, Nat. Commun. **6**, 7565 (2015).
[40] See Supplemental Material http://link.aps.org/supplemental/10.1103/PhysRevLett.127.013901 for (i) the effective Hamiltonian around the Weyl point (WP), (ii) another WP related to $B(B')$ waveguides, (iii) Fermi arclike edge states related to a single WP, (iv) symmetry analysis of the WP in the parameter space, (v) Geometric interpretation of the rotation in the parameter space, (vi) two WPs rotating in the opposite directions, (vii) eigenvalue spectrum as a function of the rotational angle φ_1 for different values of θ, (viii) two WPs rotating in the same direction, (ix) sample fabrication and measurement, (x) propagation simulations for the three samples with long distance and disorders, and (xi) propagation simulations showing the adiabatic process with different φ_1 s for the loop $\varphi_2 = -\varphi_1 - 0.1\pi$, which includes Refs. [41,42].
[41] H. B. Nielsen and M. Ninomiya, Nucl. Phys. **B185**, 20 (1981).
[42] D. N. Christodoulides, F. Lederer, and Y. Silberberg, Nature (London) **424**, 817 (2003).
[43] Z. Fang *et al.*, Science **302**, 92 (2003).
[44] Q. Wang, K. Ding, H. Liu, S. Zhu, and C. T. Chan, Opt. Express **28**, 1758 (2020).